COBEM 2021 26th International Congress of Mechanical Engineering
November 22-26, 2021, Virtual Congress, Brazil

# COB-2021-1275
# HEMODYNAMICS STUDY OF BLOOD AND SENSITIVITY ANALYSIS IN BIOLOGICAL STRUCTURE FOR CASES OF ISCHEMIC STROKE

**Tarik Hazem Ashmawi**
**João Pedro de Oliveira Donato**
**Alessandro Baccaro Filho**
**Beatriz Ikeda Alcatrão**
**Bruno Galelli Chieregatti**
**João de Sá Brasil Lima**
Instituto Mauá de Tecnologia (IMT), Praça Mauá,1 – Mauá, São Caetano do Sul. CEP: 09580-900
tarik.ashmawi@gmail
joao.o.donato@hotmail.com
Alessandro.Baccaro@hotmail.com
beatrizikeda33@gmail.com
bruno.chieregatti@maua.br
joao.brasil@maua.br

**Carlos Eduardo Baccin**
Hospital Israelita Albert Einstein, Av. Albert Einstein, 627 – Jardim Leonor, São Paulo – CEP: 05652-900
cebaccin@gmail.com

***Abstract.*** *According to the Brazilian Ministry of Health, over 101 thousand deaths registered in 2020 were caused by stroke, a disease that can be classified as hemorrhagic or ischemic with the last one being the cause of over 80% of all cases. For such reason it shall be the topic of focus of this study. The ischemic stroke is consequence of a blockage inside one of the blood vessels leading to the brain, decreasing blood flow which may result in lack of oxygen and nutrients to the cerebral tissue. The main causes of an ischemic stroke are the presence of either an atherosclerotic plaque, composed of the accumulation of lipids or fibrous matter; or a thrombus, the latter occurring in regions already obstructed by the former and being made of blood clot particles. Seeking to further comprehend human health, medicine and engineering have been working together, for example, to study biological flows. Such union between the two areas paves the way for more effective solutions. Ischemic stroke itself is an example of a disease that is under study in order to make its identification more agile, as well as its stage and provide increasingly less invasive prophylaxis. Thus, the main goal of this work is directed towards obtaining the relevant parameters involved in the hemodynamics within the internal carotid artery (ICA) in the cranial section affected by an ischemic stroke. Blood flow will be analyzed using a computer fluid dynamics (CFD) simulation with the Ansys Fluent software to solve the three-dimensional Navier–Stokes equation, while vessel geometry will be modeled and based on real data. Different instances will be studied: first a healthy artery and then one with varying degrees of stenosis from 50% to 90% of obstruction. Through these stenosis variations, existing correlations between some parameters will be analyzed through a sensitivity analysis, such as: pressure gradient, wall shear stress and flow velocity. The main goal of this work is to analyze the blood flow through an internal carotid artery affected by an ischemic stroke with different degrees of obstruction and compare the results using both Newtonian blood model and non-Newtonian Carreau-Yasuda model.*

***Keywords:*** *internal carotid, CFD simulation, ischemic stroke, velocity, pressure*

## 1. INTRODUCTION

A stroke is a cerebrovascular disease because it affects both the encephalic (brain) area and the blood vessels (vascular) that supply blood to the brain. According to the World Health Organization (WHO), the disease refers to the rapid development of clinical signs of focal and/or global disturbances of brain function, with symptoms lasting 24 hours or more, of vascular origin, where they cause alterations in the cognitive and sensory-motor plans, according to the area and extent of the lesion. Despite the stroke pathophysiology, it results in irreversible damage to neurons and subsequent major neurological deficits. Brain ischemic stroke is one of the leading causes of morbidity and mortality in developed countries. The World Health Organization ranks stroke as the second leading cause of death in the world, second only to ischemic heart disease.

A stroke can be subdivided into two types: ischemic stroke and hemorrhagic. In the first condition, blood inflow is impaired or absolutely blocked due to an occlusion of the supplying artery. The results of an ischemic stroke on cerebral

tissue can be observed on Figure 1. CET scan of an ischemic stroke on the right middle artery. The region affected by lack of blood flow is presented with a darker grey.(Bajaj et al, 2018), where the dark grey regions represent the infarcted brain sections, due to loss of blood supply. The degree of ischemic injury is related to the duration and severity of the reduction in flow, as well as to the presence of collateral circulation, which is a type of circulation in which there is communication between the arteries and veins to serve as a detour to the flow. On the other hand, the second type is due to a rupture of the blood vessel, and its most frequent cause is arterial hypertension. However, it is responsible for only about 10% of all strokes.

Bioengineering is the union of two essential areas for human development, namely engineering and biology. Its rapid progress and greater exploration have and continue to contribute positively in the health field, through new treatments, as well as greater precision and effectiveness.

Blood is a fluid present in the cardiovascular system and is always in a unidirectional movement. It presents a biphasic mixture that comprises several types of formed elements (red blood cells, white blood cells, platelets) suspended in an aqueous solution of organic molecules, proteins and salts called plasma. Due to this multicomponent nature, blood exhibits complex rheological properties. What makes it a challenge in studies is the fact that it does not meet Newton's Law of Viscosity. It is defined as a non-Newtonian fluid because its fluid properties are not described with a constant viscosity value and the relationship between strain rate and shear stress is non-linear (Fatahian, 2018). In particular, several experimental investigations have shown that blood has the so-called thinning behavior, that is, its viscosity decreases with increasing shear rates (Guerciotti, 2017).

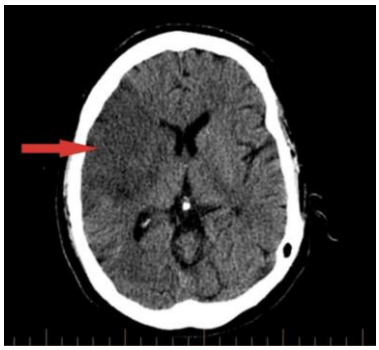

Figure 1. CET scan of an ischemic stroke on the right middle artery. The region affected by lack of blood flow is presented with a darker grey. (BAJAJ et al, 2018)

The Computational Fluid Dynamics (CFD) technique is a useful mathematical tool for hemodynamic investigation (Paliwal, 2017). It enables assessment of the diseases severity and improves planning of the reconstructive surgery (Liu, 2013). Preoperatively created 3D vascular models can be used to predict the hemodynamics and optimize the surgery plans (Zhang, 2016).

The computer code is capable of solving a system of coupled differential or integral equations with a properly posed set of initial and/or boundary conditions correctly and reproduces the exact solution to these equations when sufficiently fine grid resolution both in time and space is employed. Before any discretization error estimation is calculated, it must be shown that iterative convergence is achieved with at least three (preferably four) orders of magnitude decrease in the normalized residuals for each equation solved. (Procedure for Estimation and Reporting of Uncertainty Due to Discretization in CFD Applications, 2008).

The recommended method for discretization error estimation is the Richardson extrapolation (RE) method. The limitations, however, of the RE method are well known. The local RE values of the predicted variables may not exhibit a smooth monotonic dependence on grid resolution, and in a time-dependent calculation, this non-smooth response will also be a function of time and space. Nonetheless, it is currently the most reliable method available for the prediction of numerical uncertainty. (Procedure for Estimation and Reporting of Uncertainty Due to Discretization in CFD Applications, 2008).

With the application of the CFD technique, the present study aims to analyze the variation in hemodynamic parameters in different degrees of obstruction in the internal carotid artery.

## 2. MATERIALS AND METHODS

### 2.1 Geometry

The repository “AneuriskWeb” was employed in order to obtain a real-life artery model for the simulations. The website itself contains a series of collected aneurysm cases, including DICOM images, between 2005 and 2008 by the

MOX Laboratory of the Mathematics Department of Politecnico di Milano. The DICOM image containing the surface was extracted and read using the vascular modeling software VMTK® (Vascular Modeling Toolkit).

The geometry from Figure 2, due to it representing an aneurysm case, needed to be modified in order be applied to this work. Firstly, its aneurismatic sack was removed through use of the VMTK software (resulting geometry is on Figure 3 [A]) with a patch added to cover the gap (Figure 3 [B]). Using the open-source software Blender, finishing on the outlines of the geometry were improved (Figure 3 [C]) and further imperfections were corrected with VMTK once again (Figure 3 [D]). The final geometry was used for the mesh convergence analysis detailed in the topic 2.3.

The CAD geometry was modelled in SolidWorks and represented a more simplified version of the original one, several ramifications were removed, leaving only one bifurcation at the upper edge. A healthy artery model was made for comparison, displayed on Figure 4 [A]; and the stenosis were produced by reducing the diameter around the middle of the section. 50%,70% and 90% stenosis arteries are present on Figure 4 [B], [C] and [D] respectively.

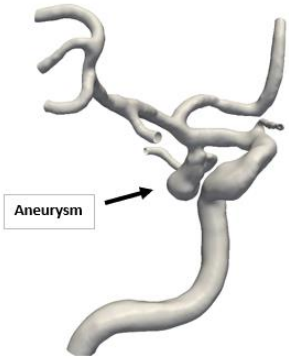


Figure 2. Image of case C0031 available on the AneuriskWeb Website

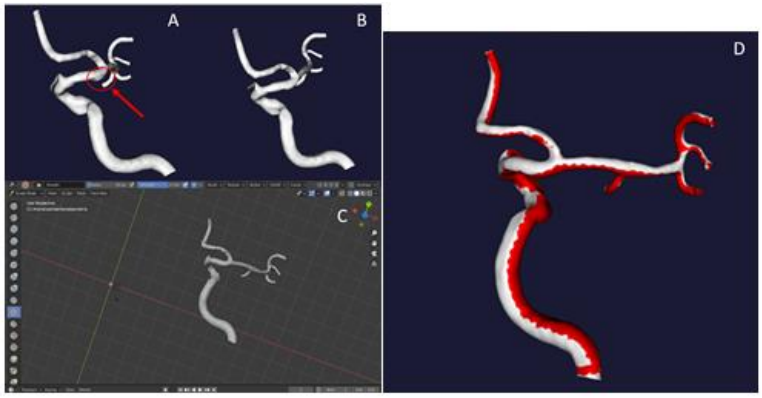


Figure 3. [A] Artery geometry after removing aneurismatic sack. A small gap can be identified on where it used to be. [B] Resulting geometry with gap closed. [C] Use of Blender software for improving finishing around geometry surface. [D] Final surface of internal carotid with newly smoothed sections in highlighted in red.

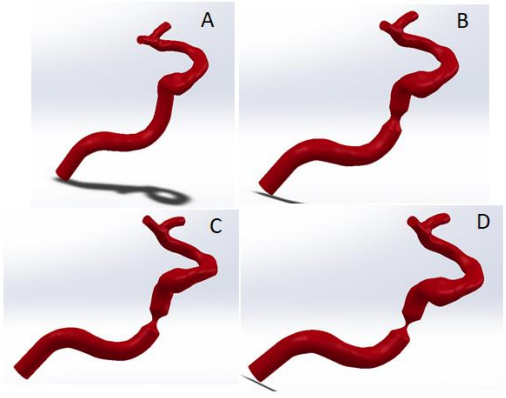


Figure 4. Internal Carotid artery geometry modeled on SolidWorks: [A] healthy artery. [B] 50% occluded artery. [C] 70% occluded artery. [D] 90% occluded artery.

### 2.2 Blood Flow Modeling

Blood flow was simulated considering constant velocity behavior valued at 0,85 m/s, obtained from data by Harloff et al (2012). In conjunction with velocity, a pressure value equal to 110 mmHg or 14,665.5 Pa is be employed at the input. (Liu et al, 2018). Blood will be assumed to be an incompressible fluid with a density equal to 1053 kg/m3, which represents a fairly common value in simulations of blood with Newtonian behavior. (Robertson, Sequeira, & Owens, 2009).

For the Newtonian cases, the dynamic viscosity was used as 0.004 kg/m.s based on the work by Shang et al (2015). The non-Newtonian simulations employed the Carreau viscosity model, described by Eq. (1), in which $\mu$ is the fluid's dynamic viscosity, $\mu_\infty$ is the viscosity at high shear rates valued at 0.0035 Pa.s, $\mu_0$, viscosity at a null shear rate of 0.056 Pa.s, $\lambda$, time constant equal to 3.313 s, $\dot{\gamma}$, shear rate; and n is the Power Law index e qual to 0.3568. (Siebert and Fodor, 2009).

$$\mu = \mu_\infty + (\mu_0 - \mu_\infty)[1 + (\lambda\dot{\gamma})^2]^{(n-1)/2} \quad (1)$$

### 2.3 Meshing

The VMTK-obtained mesh geometry was employed for the mesh discretization error estimation. Three simple simulations were created with boundary conditions considering the Newtonian blood model and constant velocity on the inlet, described in topics 2.2. Each had a different mesh, varying the element size: the fine mesh had an average element size of 0,10 mm (Figure 5 [A]), the medium one, 0,15 mm (Figure 5 [B]) and coarse, 0,20 mm (Figure 5 [C]). The pressure variations between the outlet and the inlet indicated in Figure 6 [A] will be the variable monitored at each simulation. Each mesh's parameters are detailed in Table 1 as well as the resulting pressure drops. The Grid Convergence Method (GCI) from Celik et al (2008) was applied and the calculated indexes are displayed on Table 2. Based on the work of Neves (2021), in case the difference between the fine and medium meshes present a GCI index lower or equal to 5%, then the medium is best for the work, since further refinements would only increase computational demand. Considering the resulting value of $GCI_{21}$ on Table 2, the chosen element size for the simulation meshes was of 0.15 mm.

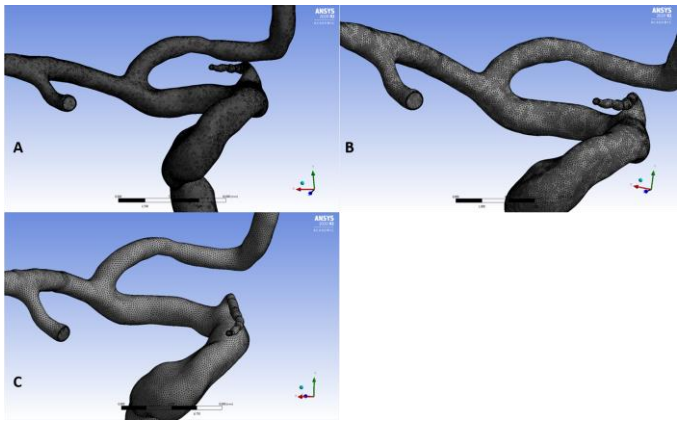


Figure 5. Three meshes generated for convergence analysis. [A] Fine. [B] Medium. [C] Coarse.

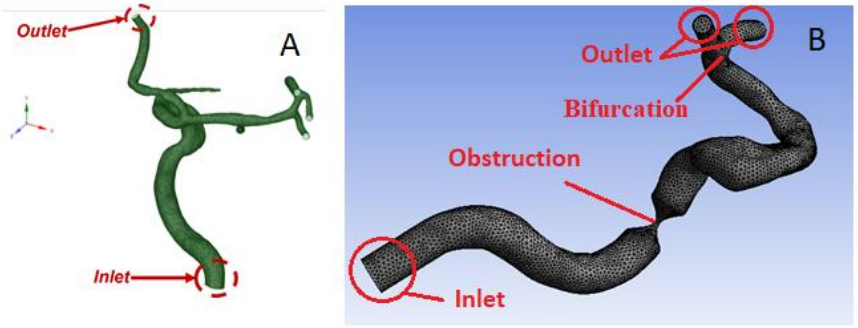


Figure 6. [A] Geometry for mesh convergence analysis and reference outlet indicated. [B] Components for the second convergence analysis

Table 1. Parameters for the mesh discretization error estimation as well as the calculated pressure drops.

| Mesh | Element Size (mm) | Number of Elements | Geometry volume or area | Inflation (boundary layer) | | Pressure drop (Pa) |
|---|---|---|---|---|---|---|
| | | | | Number of layers | Maximum thickness | |
| Fine | 0,08 | 8394618 | 1279,37 | 10 | 0,12 | -9668,50 |
| Medium | 0,15 | 2490265 | | | | -9516,64 |
| Coarse | 0,20 | 1111040 | | | | -9266,82 |

Table 2. Grid Convergence Method indexes for each pair of meshes: 21 represents the fine and medium ones, while 32 is the medium and coarse pair.

| | |
|---|---|
| $GCI_{21}$ = | 0,944% |
| $GCI_{32}$ = | 2,953% |

The mesh convergence analysis model described was used only for the healthy and 70% obstructed geometry. For the 50% and 90% obstructed models, a different analysis was necessary, since both presented program constraints when generating the mesh on the Ansys "mesh" platform. The 90% obstructed artery is described as the most critical scenario, since its structure presents a sharp reduction in diameter. Therefore, the second convergence analysis was performed only on it, since the results can be valid for the 50% blocked geometry. The mesh change was divided into 2 regions: the first was in the obstructed region, where the "sizing" command was applied, and the second was at the bifurcation, where an influence sphere was used. In all, 7 simulations were performed, where was tried to follow a pattern in changing the size of the element from one mesh to another, to allow a better comparison between the results. However, due to software errors when generating the mesh, in some cases it was necessary to make minor changes in the values, to obtain the mesh.

Table 3. Number of elements and volume geometry for the three meshes.

| Mesh | Element Size body (mm) | Element Size in Stenosis (mm) | Element size Bifurcation (mm) | Number of Elements | Pressure drop (Pa) |
|---|---|---|---|---|---|
| Mesh 1 | 0,4 | 0,160 | 0,260 | 232.268 | -1,42156e+06 |
| Mesh 2 | 0,4 | 0,175 | 0,275 | 217.692 | -1,13028e+06 |
| Mesh 3 | 0,4 | 0,200 | 0,300 | 201.692 | -1,18955e+06 |
| Mesh 4 | 0,4 | 0,225 | 0,325 | 187.983 | -1,38951e+06 |
| Mesh 5 | 0,4 | 0,250 | 0,350 | 180.884 | -1,45581e+06 |
| Mesh 6 | 0,4 | 0,278 | 0,378 | 175.027 | -1,50732e+06 |
| Mesh 7 | 0,4 | 0,300 | 0,400 | 170.712 | -1,50814e+06 |

The comparison between the results was based on the pressure drop parameter, which refers to the pressure difference between the "Outlet" and "Inlet" region of the artery, as shown in Figure 6 [B]. It is noticeable that the number of elements in a mesh interferes directly in the results, although there is no proportionality regarding how much the change alters in the post-simulation. In this case, a pattern was found whereas the number of elements decreases, the head loss increases. Convergence was evident in mesh 6, where the difference to mesh 7 was minimal. Therefore, it was used in the 50% and 90% obstructed geometry for the following simulations.

## 3. SIMULATIONS AND RESULTS

For all simulations, hybrid versions and a value of 150 interactions were used. The parameters analyzed at the end of the simulation were: pressure and velocity, where the critical location for such analyses was in the region of obstruction. For the analysis, a longitudinal axis was designed around such region and the pressure and velocity values were measured for each geometry. In the case of the healthy artery, the line was constructed on the corresponding section of the geometry where the stenosis would have been.

- **Pressure drop across stenosis: non-Newtonian and Newtonian models**

Analyzing the pressure graphs obtained for both models, Newtonian on Figure 8 and non-Newtonian, Figure 7 the behavior detected is nearly identical with very subtle differences on the 70% obstructed geometries: the values at the

entrance of the stenosis are around 7.9 kPa and 8.2 kPa for the non-Newtonian and Newtonian models respectively, as well as on the exit: 3.2 kPa and 3.6 kPa.

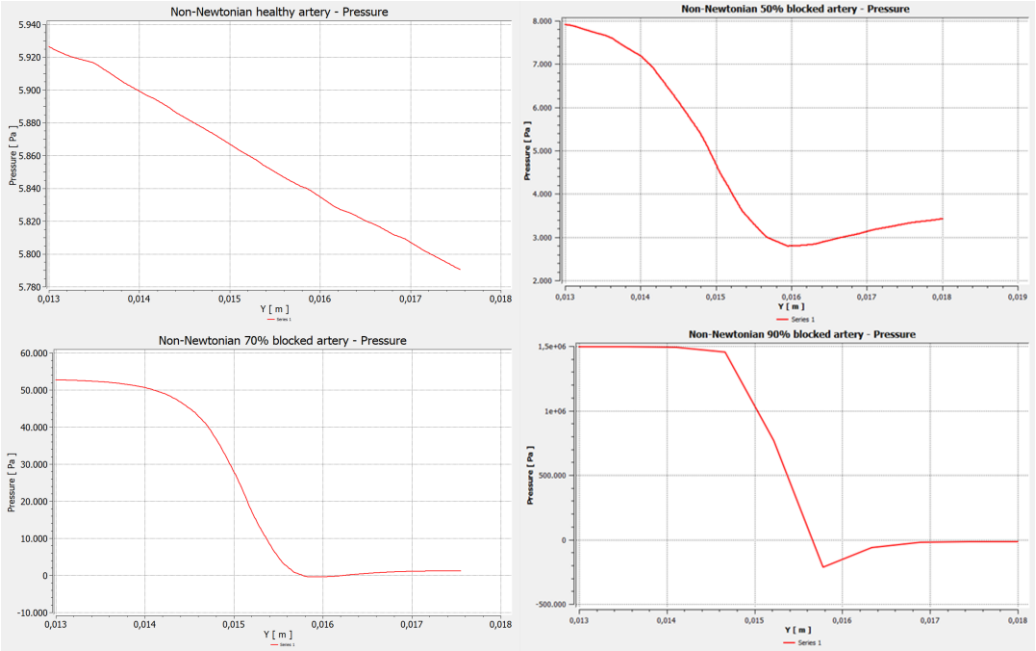


Figure 7 Pressure graphs along the stenosis section within the geometries obtained by the non-Newtonian CFD simulations. Upper left: healthy artery (geometry section corresponding to stenosis location on obstructed arteries, upper right: 50% obstructed artery, lower left: 70% obstructed artery and lower right: 90% obstructed artery.

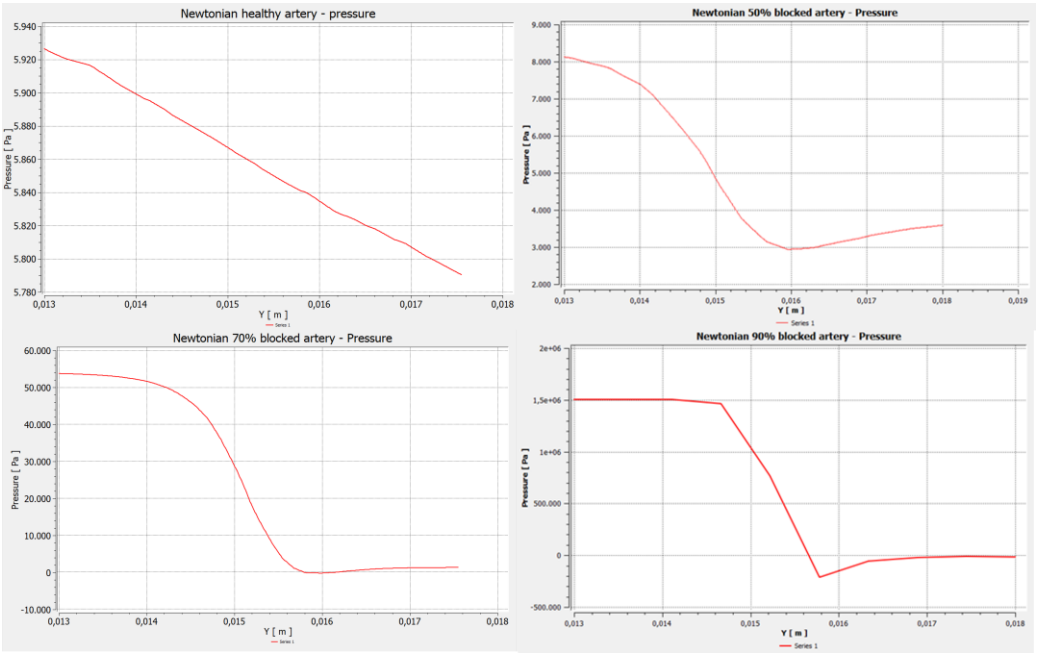


Figure 8. Pressure graphs along the stenosis section within the geometries obtained by the Newtonian CFD simulations. Upper left: healthy artery (geometry section corresponding to stenosis location on obstructed arteries, upper right: 50% obstructed artery, lower left: 70% obstructed artery and lower right: 90% obstructed artery.

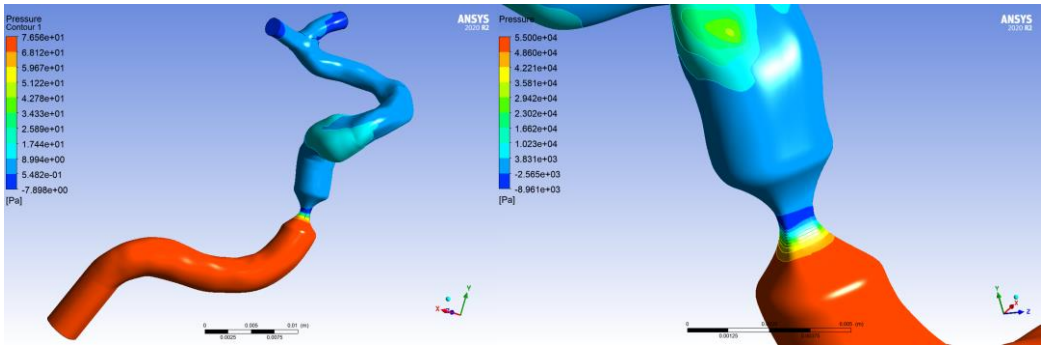


Figure 9. Pressure contour graph of 70% obstructed artery using a Newtonian simulation. Left: overall view of contour, right: close-up of obstructed area.

On Figure 9 above, a contour graph detailing the pressure across the 70% obstructed geometry using the Newtonian blood model can be observed. On the close-up of the stenosis (right figure), a gradual variation in pressure occurs as the fluid passes through the obstruction.

- **Velocity variation across stenosis: non-Newtonian and Newtonian models**

The same can be described for the velocities (Figure 10 and Figure 11 are respectively for the non-Newtonian and Newtonian models) with discreet discrepancies on the 70% geometries too. The peak velocity for the Newtonian graph was of 10.2 kPa, while 10.1 kPa was detected with the non-Newtonian model; and 10.0 kPa was the value at the end of the stenosis for the Newtonian with the Newtonian model being slightly under 10.0 kPa.

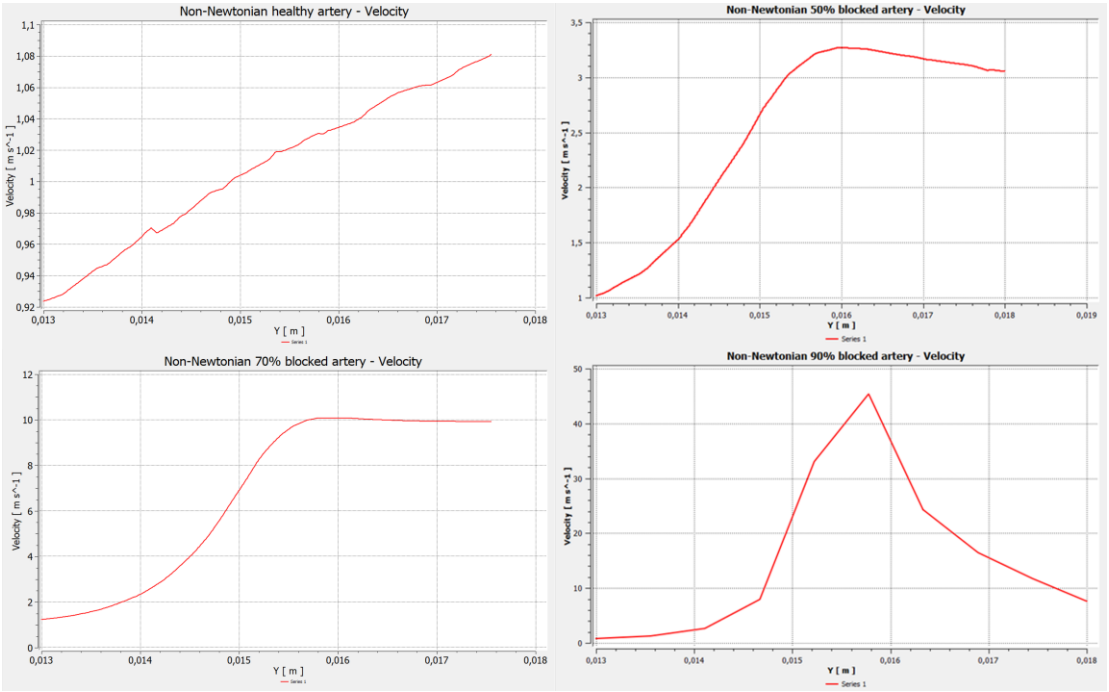


Figure 10. Velocity graphs along the stenosis section within the geometries obtained by the non-Newtonian CFD simulations. Upper left: healthy artery (geometry section corresponding to stenosis location on obstructed arteries, upper right: 50% obstructed artery, lower left: 70% obstructed artery and lower right: 90% obstructed artery.

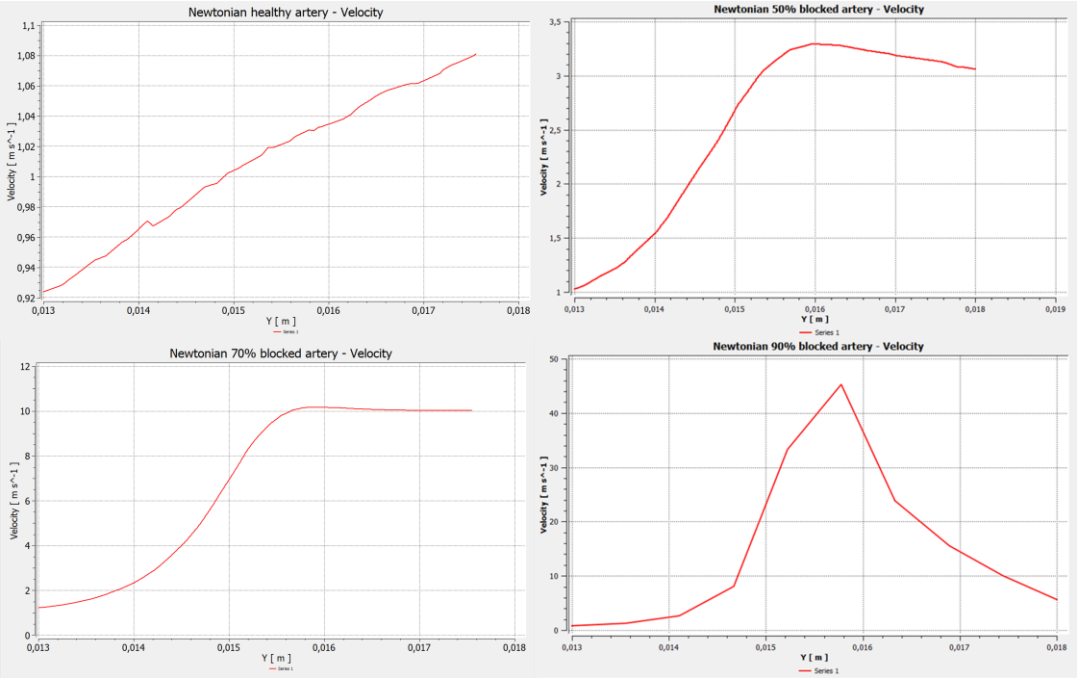


Figure 11. Velocity graphs along the stenosis section within the geometries obtained by the Newtonian CFD simulations. Upper left: healthy artery (geometry section corresponding to stenosis location on obstructed arteries, upper right: 50% obstructed artery, lower left: 70% obstructed artery and lower right: 90% obstructed artery.

On Figure 12, the trajectory of the current lines is uniform and constant until it meets the blocked section of the artery. Once the diameter of the section decreases, in other words, once the blood meets the 90% stenosis, its velocity starts to rise and its flow becomes disturbed.

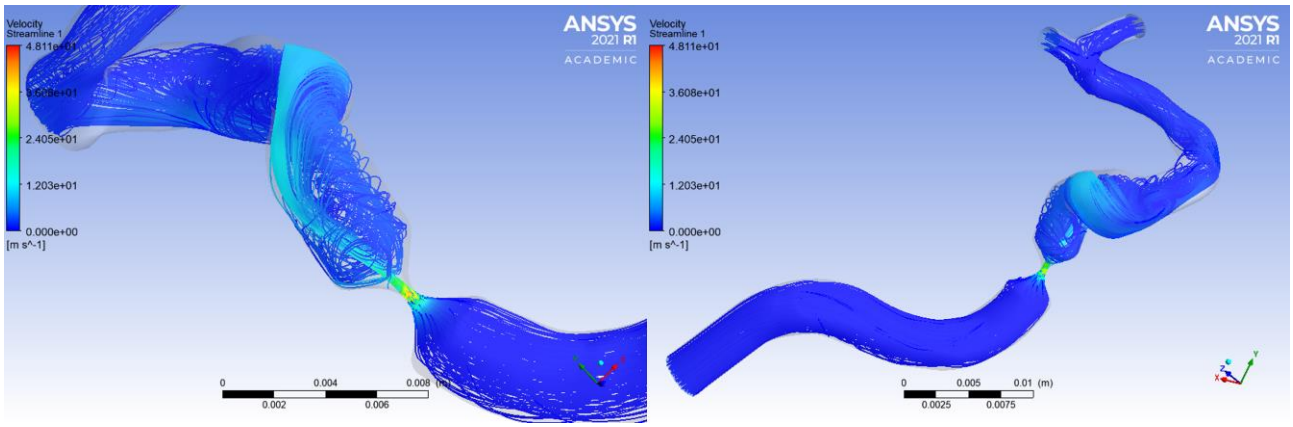


Figure 12. Streamline graph of 90% obstructed artery using a non-Newtonian simulation. Left: close-up of obstructed area, right: overall view of contour.

Considering the evident and near identical behaviors of velocity and pressure on the studied sections of the geometries for both Newtonian and -non-Newtonian, the discussion of the effects of the obstruction shall be centered around the former due to its simplicity in blood modelling, since the viscosity is deemed constant.

Firstly, linear tendencies are noticed on the pressure and velocity curves for the healthy artery (upper right on Figure 8 and on Figure 11 respectively). The former can be approximated by the Eq. (2), increasing along the stenosis; and the latter, Eq. (3), decreasing; “X” being the position across the X-axis.

$$p = -29750X + 6312.7 \quad (2)$$

$$V = 36{,}667X + 0{,}4483 \quad (3)$$

Such inversely proportional behavior between velocity and pressure, as well considering that blood as an incompressible fluid with the Newtonian model and the flow as a steady state through the constant velocity and pressure at the inlet the topic can evaluated using the Bernoulli equation as presented on Eq. (4), the height differences can be disregarded, due to being very small in comparison to the pressure and velocity values. (Munson, Young, Okiishi, 2004)

$$\mathrm{p} + \frac{1}{2}\rho V^2 = constant \tag{4}$$

With both parameters, such linear behaviors are eliminated with the presence of a stenosis, which hampers the prediction of values along the obstructed geometry.

The pressure on the 50% obstructed artery (upper right on Figure 8) descends until reaching its lowest value of 2.8 kPa on 0.016 m within the stenosis and begins then increasing on much lower rate, which differs from the behavior observed on the healthy artery. Similarly, the 70% obstructed displays a decrease in pressure up to 0.01585 m with a low-rate increase in value. The main difference is on the value range: while the 50% obstructed artery had a maximum and minimum pressures of 8.2 kPa and 3.0 kPa, the 70% case's pressure is within 0-54 kPa, a rise of 980% in range size. For the 90% obstructed artery (Figure 7), the pressure range size increases then in 3.518.5%: [-400, 1500] kPa. The pressure is near constant on the stenosis until 0.01415 m, after which begins a decrease at a low and linear rate to 0.01465 m, then at a much higher rate until reaching its lowest value of -400 kPa at 0.0158 m. The curve then rises until settling at a constant value of 0 kPa after reaching 0.017 m.

Observing the velocity graphs for the obstructed arteries (upper right, lower left and lower right on Figure 11), the behavior governed by the Bernoulli equation can once again be observed: the peak and lowest values as well as decreasing and increasing curve behaviors are all in line with pressure graphs.

The graphs on (Figure 10) indicate an increase in peak velocity near the stenosis with the obstruction size, varying from 3.3 to 10.25 and then 46 m/s for 50, 70 and 90% obstructed geometries respectively. Therefore, a decrease in the overall cross-sectional area, in this case, a stenosis, causes a great rise in the blood's velocity profile which correspondingly affects the pressure behavior.

## 4. CONCLUSIONS

This paper has generated a comparative study between Newtonian and non-Newtonian blood models for modeling an internal carotid artery affected by an ischemic stroke with different degrees of obstruction. Both models, when applied to all geometries from the healthy artery to the 90% obstructed one, have displayed near identical results with subtler differences visible on the 70% occluded geometry. For practical reasons, the preferable model for evaluating blood behavior in this vessel in such conditions is the Newtonian one, since the analysis is simplified by discarding the use of a non-Newtonian governing model, such as the Carreau model, in which parameters as the Power Law index and viscosity at high shear rates are not required.

For healthy arteries, both parameters, velocity as well as pressure exhibit linear behaviors. Such phenomena enable prediction of velocity and pressure values along the internal carotid vessel by employing a linear and the Bernoulli equation, when considered a steady-state flow and disregarding the height differences among sections of the artery. When dealing with occlusions, the linear behavior is ceased and both parameters exhibit an inversely proportional correlation.

Pressure range increases greatly with bigger occlusion sizes and vacuum can be obtained within the artery when near to 90% of its cross-section is obstructed. However, the pressure values tend to stabilize quicker in latter cases. Peak velocities are also higher in arteries more obstructed due to stronger diameter variation.

For further and future, the pulsatile blood flow should be considered in order to better model the cinematics behind.

## 5. REFERENCES

Bajaj, D.; Agrawal, A; Gupta, S.; Bajaj, S. Recreational Nitrous Oxide Abuse Causing Ischemic Stroke in a Young Patient: A Rare Case Report. Cureus 10(12): e3761, December, 2018.

Celik, I. B.; Ghia, U.; Roache, P. J.; Freitas, C. J.; Coleman, H.; Raad, P. E. Procedure for Estimation and Reporting of Uncertainty Due to Discretization in CFD Applications. Journal of Fluids Engineering, v. 130, n. 7, July 2008.

Fatahian, E.; Kordani, N.; Fatahian, H. The Application of Computational Fluid Dynamics (CFD) Method and Several Rheological Models of Blood Flow: A Review. Journal of Science, v. 31, n. 4, p. 1213-1227, July 2018.

Guerciotti, B.; Vergara, C. Computational Comparison Between Newtonian and Non-Newtonian Blood Rheologies in Stenotic Vessels. Biomedical Technology, v. 84, p. 169-183, August 2017.

Harloff, A.; Zech, T.; Wegent, T.; Strecker, C.; Weiller, C.; Markl, M. Comparison of Blood Flow Velocity Quantification by 4D Flow MR Imaging with Ultrasound at the Carotid Bifurcation. American Journal of Neuroradiology, e. 34, p. 1407-1413. July 2012.

Hospital Brasília, 2020. Every six seconds someone, somewhere, dies of a stroke (in Portuguese). Equipe Hospital Brasília, https://hospitalbrasilia.com.br/pt/sobre-nos/blog/a-cada-seis-segundos-alguem-em-algum-lugar-morre-de-avc. Accessed on 20th of July, 2021.

Kreith, F.; Goswami, D. Y.; Sandor, B. I. Thermal Conductivity Data for Specific Tissues and Organs for Humans and Other Mammalian Species. In: CRC Handbook of Mechanical Engineering. CRC Press, 2004, chapter 4.

Liu, J.; Sun, Q.; Qian, Y.; Hong, H.; Liu, J. Numerical simulation and hemodynamic analysis of the modified Blalock-Taussig shunt. Conf. Proc. Annu. Int. Conf. IEEE Eng. Med. Biol. Soc. IEEE Eng. Med. Biol. Soc. Annu. Conf. 2013, 2013, 707–710.

Munson, B. R.; Young, D. F.; Okiishi, T. H. Fundamentos da Mecânica dos Fluidos. São Paulo: Blucher, 4th ed., 2004.

Liu, H. et al. Impact of Side Branches on the Computation of Fractional Flow in Intracranial Arterial Stenosis Using the Computational Fluid Dynamics Method. Journal of Stroke and Cerebrovascular Diseases, Hong Kong, v. 27, n. 1, p. 44-52, January 2018.

Neves, M. D. C. Análise de Malha pelo Método GCI. Linkedin, 2020. Available at: <https://www.linkedin.com/pulse/an%C3%A1lise-de-malha-pelo-m%C3%A9todo-gci-marcus-godolphim-de-castro-neves/?originalSubdomain=pt>. Accessed on 25th of July, 2021.

Paliwal, N.; Damiano, R.J.; Varble, N.A.; Tutino, V.M.; Dou, Z.; Siddiqui, A.H.; Meng, H. Methodology for computational fluid dynamic validation for medical use: Application to intracranial aneurysm. J. Biomech. Eng. 2017, 1, 139.

Procedure for Estimation and Reporting of Uncertainty Due to Discretization in CFD Applications. Journal of Fluids Engineering, v. 130, n. 7, July 2008

Robertson, A. M; Sequeira, A.; Owens, R. G. Rheological models for blood. Cardiovascular Mathematics. Milan, 2009, vol. XII, 211-241.

Siebert, M. W.; Fodor, P. S. Newtonian and Non-Newtonian Blood Flow over a Backward Facing Step - A Case Study. COMSOL. Boston, 2009.

Sinnot, M.; Cleary, P. W.; Prakash, M. An investigation of pulsatile blood flow in a bifurcating artery using a grid-free method. Fith International Conference of CFD in the Process Industries CSIRO, Melbourne, Australia, 2006.

Shang, E. K.; Nathan, D. P.; Fairman, R. M.; Bavaria, J. E.; Gorman, R. C.; Gorman III, J. H.; Jackson, B. M. Use of computational fluid dynamics studies in predicting aneurysmal degeneration of acute type B aortic dissections. Journal of Vascular Surgery. Philadelphia, Seattle, 2015, 1-6.

Zhang, W.; Liu, J.; Yan, Q.; Liu, J.; Hong, H.; Mao, L. Computational haemodynamic analysis of left pulmonary artery angulation effects on pulmonary blood flow. Interact. Cardiovasc. Thorac. Surg. 2016, 23, 519–525.

## 6. RESPONSIBILITY NOTICE

The author(s) is (are) the only responsible for the printed material included in this paper.